

# Lattice Boltzmann study of capillary forces between cylindrical particles

HIROYUKI SHINTO \*, DAISUKE KOMIYAMA and KO HIGASHITANI

*Department of Chemical Engineering, Kyoto University, Nishikyo-ku, Kyoto 615-8510, Japan*

Received 1 May 2007; accepted 19 June 2007

**Abstract**—In the present study, numerical simulations based on a two-dimensional two-phase lattice Boltzmann (LB) method have been performed to examine two types of capillary forces: (i) the lateral capillary force between two horizontal cylinders of wetting and/or non-wetting surfaces trapped at a liquid–vapor interface, and (ii) the capillary bridge force between the two wetting cylinders covered with liquid films in vapor. The force–distance profiles for these two systems agree well with those from the corresponding theoretical descriptions, indicating that the present LB simulation can reproduce the capillary forces between two bodies with various wettabilities.

**Keywords:** Lattice Boltzmann method; multiphase fluid; colloidal particles; lateral capillary force; capillary bridge force; wettability.

## 1. INTRODUCTION

Interactions between particles at fluid interfaces are often mediated by capillary forces, which have been mechanistically classified into the lateral capillary force and the capillary bridge force. The former is caused by the overlap of menisci formed around separate particles attached to an interface, while the latter arises from the capillary bridge of a second phase between particles immersed in a bulk medium of another phase. These forces have drawn an increasing interest of those working in the field of materials science and engineering as they are important for the self-assembly of particles ranging in size from millimeters down to nanometers, including protein molecules [1–4]. Both the lateral capillary force and the capillary bridge force have been extensively studied in terms of experiments and theories [1–3]. As a result, some theoretical expressions successfully reproduce these capillary forces between two particles mediated by mechanically equilibrated interfaces (i.e. the two-body hydrostatic capillary forces) [1–3]. However, it is

---

\*To whom correspondence should be addressed. E-mail: [shintou@cheme.kyoto-u.ac.jp](mailto:shintou@cheme.kyoto-u.ac.jp)

rather difficult to take into account the many-body effects [5] and the hydrodynamic effects [6] on the capillary forces using their theoretical expressions.

Numerical simulations based on the lattice Boltzmann (LB) methods are a good tool to reproduce fluid flows in the presence of solid bodies of various shapes [7–10]. Ladd proposed a technique to simulate the mobile particles in a single-phase flow, where the particles are mapped onto the lattice grid and then a net momentum transfer between the fluid and the solid sites is integrated to obtain the force and the torque acting on a particle [11, 12]. This technique has been refined in Refs [13–15]. Recently, the refined technique [15] was extended to the binary fluid problems, such as a single particle at a fluid–fluid interface [16, 17] a particle-coated fluid cylinder [17, 18] and the spinodal decomposition in the presence of particles [19]. To our best knowledge, however, no LB studies have reported the force–distance profiles for the capillary forces between solid bodies in two-phase fluids, except our recent contribution [20].

In the present study, two distinct systems are investigated: (i) two cylindrical bodies trapped at the liquid–vapor interface in mechanical equilibrium, where the two bodies deform the interface to experience the lateral capillary force, and (ii) two cylindrical bodies covered with the mechanically equilibrated liquid films in the vapor, where the two bodies at small separations hold the liquid bridge in their gap to feel the capillary bridge force. These two systems have been simulated by a two-phase liquid–vapor LB method, where the capillary forces between two cylindrical bodies are calculated as a function of the separation distance. The results are compared with those from the theoretical expressions.

## 2. SIMULATION METHODS

In the present investigation, we consider two systems: (A) two solid bodies that are trapped on the surface of a dense liquid under gravitation (Fig. 1), and (B) two solid bodies covered with the liquid films that are placed in the vapor with no gravity (Fig. 2). The lateral capillary forces were evaluated for system A, while the capillary bridge forces were calculated for system B.

### 2.1. Two-phase liquid–vapor flows

For simulating two-phase flows, several LB methods have been described, such as the chromodynamic model [21, 22], the pseudopotential model [23, 24], the free-energy model [25, 26] and the index fluid method developed from the free-energy model [27, 28]. The latter method [28] was adopted in the present study.

Hereafter, we use non-dimensional variables, which are defined by using the characteristic quantities of length  $L_0$ , flow speed  $U_0$ , particle speed  $c$ , time scale  $t_0 (=L_0/U_0)$  and reference density  $\rho_0$ . The two-dimensional nine-velocity (D2Q9) model was employed, where the physical space of interest is divided into a square lattice and the evolution of the particle population at each lattice site is computed.

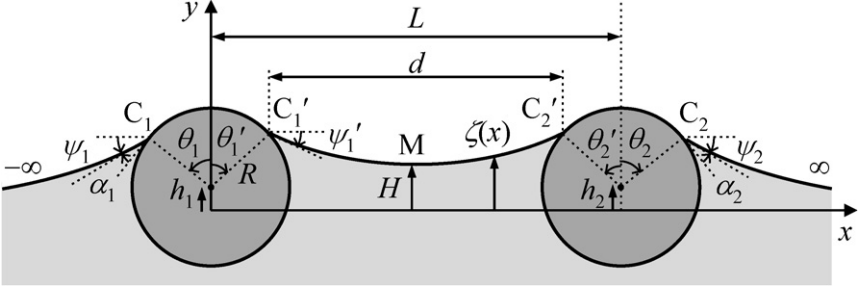


**Figure 1.** Sketch of two horizontal cylinders of radius  $R$ , which are vertically constrained at the interface between vapor and liquid phases, and separated at a center-to-center distance  $L$ .  $\zeta(x)$  is the shape of the meniscus formed around the cylinders,  $h_i$  is the vertical position of the central axis of cylinder  $i$  ( $=1$  or  $2$ ) with respect to the level  $y = \zeta(\pm\infty) \equiv 0$  of the non-disturbed horizontal interface far from the cylinders, and  $H = \zeta(L/2)$ .  $\alpha_i$  is the three-phase contact angle,  $\psi_i (\equiv \theta_i - \alpha_i)$  and  $\psi'_i (\equiv \theta'_i - \alpha_i)$  are the slope angles of the exterior and the interior menisci, respectively, and  $d$  is the horizontal distance between the contact lines  $C'_1$  and  $C'_2$  of the interior meniscus.

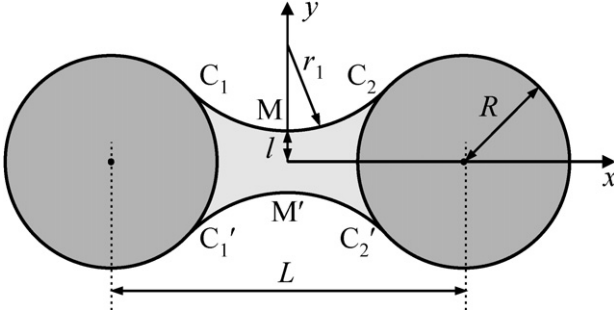


**Figure 2.** Sketch of the capillary bridge of a liquid phase between two cylinders of radius  $R$  in a vapor phase, which are identical and separated at a center-to-center distance  $L$ .  $r_1$  is the radius of curvature of the bridge and  $l$  is the half thickness of the bridge at the cross-section  $MM'$ .

The D2Q9 model has velocity vectors  $\mathbf{c}_i = (0, 0), (1, 0), (0, 1), (-1, 0), (0, -1), (1, 1), (-1, 1), (-1, -1)$  and  $(1, -1)$  for  $i = 1, 2, \dots$ , and  $9$ , respectively. In the two-phase liquid–vapor LB method [28], the coexistence of the liquid phase of density  $\rho_L$  with the vapor phase of density  $\rho_V$  is assumed, and two particle distribution functions,  $f_i$  and  $g_i$ , are used.

The distribution functions,  $f_i(\mathbf{x}, t)$  and  $g_i(\mathbf{x}, t)$  with velocity  $\mathbf{c}_i$  at node  $\mathbf{x}$  and at time  $t$ , evolve following:

$$f_i(\mathbf{x} + \mathbf{c}_i \Delta x, t + \Delta t) = f_i(\mathbf{x}, t) - \frac{1}{\tau_f} [f_i(\mathbf{x}, t) - f_i^{\text{eq}}(\mathbf{x}, t)], \quad (1)$$

$$g_i(\mathbf{x} + \mathbf{c}_i \Delta x, t + \Delta t) = g_i(\mathbf{x}, t) - \frac{1}{\tau_g} [g_i(\mathbf{x}, t) - g_i^{\text{eq}}(\mathbf{x}, t)] - 3E_i c_{iy} (\rho - \rho_V) g \Delta x, \quad (2)$$

where  $f_i^{\text{eq}}$  and  $g_i^{\text{eq}}$  are the equilibrium distribution functions,  $\tau_f$  and  $\tau_g$  are the dimensionless single relaxation times,  $\Delta x$  is a spacing of the square lattice, and  $\Delta t \equiv (U_0/c)\Delta x$  is a time step during which the particles travel the lattice spacing. The effect of gravity is considered by the third term in the right-hand side of (2), where  $g$  is the dimensionless gravitational acceleration and  $\rho$  and  $E_i$  will be given in (6) and (9), respectively [28].

The compositional order parameter  $\phi$  distinguishing two phases, the flow velocity  $\mathbf{u}$  and the pressure  $p$ , are defined as:

$$\phi(\mathbf{x}, t) = \sum_{i=1}^9 f_i(\mathbf{x}, t), \quad (3)$$

$$\mathbf{u}(\mathbf{x}, t) = \frac{1}{\rho(\mathbf{x}, t)} \sum_{i=1}^9 \mathbf{c}_i g_i(\mathbf{x}, t), \quad (4)$$

$$p(\mathbf{x}, t) = \frac{1}{3} \left[ \sum_{i=1}^9 g_i(\mathbf{x}, t) - \rho(\mathbf{x}, t) \right], \quad (5)$$

with the density  $\rho$ :

$$\rho(\mathbf{x}, t) = \frac{\phi(\mathbf{x}, t) - \phi_V}{\phi_L - \phi_V} (\rho_L - \rho_V) + \rho_V, \quad (6)$$

where  $\phi$  ranges from the minimum  $\phi_V$  to the maximum  $\phi_L$ .

The two equilibrium distribution functions are expanded as a power series of the local velocity:

$$\begin{aligned} f_i^{\text{eq}} = & H_i \phi + F_i \left( p_0 - \kappa_f \phi \frac{\partial^2 \phi}{\partial x_\alpha^2} \right) + E_i \phi \left( 3u_\alpha c_{i\alpha} - \frac{3}{2} u_\alpha u_\alpha + \frac{9}{2} u_\alpha u_\beta c_{i\alpha} c_{i\beta} \right) \\ & + E_i \kappa_f G_{\alpha\beta}^\phi c_{i\alpha} c_{i\beta}, \end{aligned} \quad (7)$$

$$\begin{aligned} g_i^{\text{eq}} = & H_i \rho + E_i \left[ 3p + \rho \left( 3u_\alpha c_{i\alpha} - \frac{3}{2} u_\alpha u_\alpha + \frac{9}{2} u_\alpha u_\beta c_{i\alpha} c_{i\beta} \right) \right] \\ & + 2F_i \omega_g u_\alpha \frac{\partial \rho}{\partial x_\alpha} + E_i (\kappa_g G_{\alpha\beta}^\rho + \omega_g J_{\alpha\beta}^\rho) c_{i\alpha} c_{i\beta}, \end{aligned} \quad (8)$$

with:

$$\left. \begin{aligned} E_1 &= 4/9, E_2 = \dots = E_5 = 1/9, E_6 = \dots = E_9 = 1/36, \\ F_1 &= -5/3, F_i = 3E_i \text{ for } i = 2, 3, \dots, 9, \\ H_1 &= 1, H_2 = \dots = H_9 = 0, \end{aligned} \right\} \quad (9)$$

$$G_{\alpha\beta}^\phi = \frac{9}{2} \frac{\partial \phi}{\partial x_\alpha} \frac{\partial \phi}{\partial x_\beta} - \frac{9}{4} \frac{\partial \phi}{\partial x_\gamma} \frac{\partial \phi}{\partial x_\gamma} \delta_{\alpha\beta}, \quad (10)$$

$$G_{\alpha\beta}^\rho = \frac{9}{2} \frac{\partial \rho}{\partial x_\alpha} \frac{\partial \rho}{\partial x_\beta} - \frac{9}{4} \frac{\partial \rho}{\partial x_\gamma} \frac{\partial \rho}{\partial x_\gamma} \delta_{\alpha\beta}, \quad (11)$$

$$J_{\alpha\beta}^{\rho} = \frac{9}{2} \left( u_{\beta} \frac{\partial \rho}{\partial x_{\alpha}} + u_{\alpha} \frac{\partial \rho}{\partial x_{\beta}} - u_{\gamma} \frac{\partial \rho}{\partial x_{\gamma}} \delta_{\alpha\beta} \right), \quad (12)$$

$$\omega_g = \frac{1}{3} \left( \tau_g - \frac{1}{2} \right) \Delta x, \quad (13)$$

where  $\kappa_f$  and  $\kappa_g$  are the constant parameters determining the interface width and the interfacial tension, respectively [28]. In the above equations, subscripts  $\alpha, \beta$  and  $\gamma$  denote Cartesian coordinates ( $\alpha, \beta, \gamma = x, y$ ) and  $\delta_{\alpha\beta}$  is the Kronecker delta. The summation convention is applied to  $\alpha$  and  $\beta$  in (7) and (8), and to  $\gamma$  in (10)–(12). In (7),  $p_0$  is given by:

$$p_0 = \frac{\phi T}{1 - b\phi} - a\phi^2, \quad (14)$$

which is the equation of state of a van der Waals fluid with the parameters  $a, b$  and  $T$  determining  $\phi_L$  and  $\phi_V$ .

The stress tensor  $\sigma = \{\sigma_{\alpha\beta}\}$  is represented as:

$$\begin{aligned} \sigma_{\alpha\beta} = & -\frac{1}{2\tau_g} P_{\alpha\beta} - \frac{\tau_g - 1/2}{\tau_g} \sum_{i=1}^9 g_i (c_{i\alpha} - u_{\alpha})(c_{i\beta} - u_{\beta}) \\ & - \frac{\tau_g - 1/2}{6\tau_g} \left( u_{\beta} \frac{\partial \rho}{\partial x_{\alpha}} + u_{\alpha} \frac{\partial \rho}{\partial x_{\beta}} + u_{\gamma} \frac{\partial \rho}{\partial x_{\gamma}} \delta_{\alpha\beta} \right) \Delta x, \end{aligned} \quad (15)$$

where  $\mathbf{P} = \{P_{\alpha\beta}\}$  is the pressure tensor:

$$P_{\alpha\beta} = p\delta_{\alpha\beta} + \frac{2}{9}\kappa_g G_{\alpha\beta}^{\rho} = \left( p - \frac{\kappa_g}{2} \frac{\partial^2 \rho}{\partial x_{\gamma}^2} \right) \delta_{\alpha\beta} + \kappa_g \frac{\partial \rho}{\partial x_{\alpha}} \frac{\partial \rho}{\partial x_{\beta}}. \quad (16)$$

The kinematic viscosity  $\nu$  and the interfacial tension  $\gamma_{LV}$  are, respectively, given by:

$$\nu = \frac{1}{3} \left( \tau_g - \frac{1}{2} \right) \Delta x, \quad (17)$$

$$\gamma_{LV} = \kappa_g \int_{-\infty}^{\infty} \left( \frac{\partial \rho}{\partial \xi} \right)^2 d\xi, \quad (18)$$

where  $\xi$  is the coordinate normal to the interface [29].

The derivatives in the above equations are calculated using the finite-difference approximations

$$\frac{\partial \lambda}{\partial x_{\alpha}} \approx \frac{1}{6\Delta x} \sum_{i=2}^9 c_{i\alpha} \lambda(\mathbf{x} + \mathbf{c}_i \Delta x), \quad (19)$$

$$\frac{\partial^2 \lambda}{\partial x_{\alpha}^2} \approx \frac{1}{3\Delta x} \left[ \sum_{i=2}^9 \lambda(\mathbf{x} + \mathbf{c}_i \Delta x) - 8\lambda(\mathbf{x}) \right], \quad (20)$$

where  $\lambda$  indicates  $\phi$  or  $\rho$ .

The parameters in (14) were chosen as  $a = 1.0$ ,  $b = 6.7$  and  $T = 3.5 \times 10^{-2}$ , which resulted in  $\phi_L = 9.714 \times 10^{-2}$  and  $\phi_V = 1.134 \times 10^{-2}$  because of the requirements for the coexistence chemical potential at  $\phi = \phi_L$  and  $\phi_V$  [30]. The density ratio  $\rho_L/\rho_V$  was set at 5 (i.e.,  $\rho_L = 0.5$  and  $\rho_V = 0.1$ ). The other parameters used were  $\tau_f = 1.0$ ,  $\tau_g = 1.1$  and  $\kappa_g = 0.01(\Delta x)^2$  throughout the present simulations, while the different values of  $\kappa_f$  and  $g$  were employed for systems A and B as in Table 1.

## 2.2. Solid surfaces with wettability

The solid body and the solid wall of a fluid-wetting surface were modeled following [31]. The fluid densities, ranging from  $\rho_V$  to  $\rho_L$ , are assigned to the solid-side lattice nodes that are on the solid surface, and then the halfway bounce-back, no-slip boundary condition [9] is applied on the fluid-side lattice nodes that are next to the solid surface. Once the fluid densities at the solid-side nodes are given, the fluid near the solid surfaces autonomously evolves to minimize the total free energy of the system [31].

In the present study, the surface of a body or a wall was represented by a collection of the continuous lattice nodes with the identical density  $\rho_S$ ; consequently, these surfaces are chemically homogeneous. The affinity of the solid surface for fluid,  $\chi$ , is defined as:

$$\chi \equiv \frac{\rho_S - \rho_d}{\rho_L - \rho_d}, \quad (21)$$

where  $\rho_V \leq \rho_S \leq \rho_L$  and  $\rho_d \equiv (\rho_L + \rho_V)/2$ . The parameter  $\chi$  satisfies  $-1 \leq \chi \leq 1$ . The solid surface becomes more wetting with increasing  $\chi$  [31]. It should be noted that all the solid-side nodes have the same density  $\rho_L$  or  $\rho_V$  when  $\chi = 1$  or  $-1$ , which corresponds to the complete wetting or the complete non-wetting surface.

## 2.3. Force on particle

As illustrated in Fig. 3, the cylindrical body of radius  $R$  was approximately represented by a collection of lattice nodes; the outer edge is not smooth but rather rough stepwise [11–19]. Following Ref. [32], the force acting on cylindrical body  $i$ ,  $\mathbf{F}_i$ , was calculated by:

$$\mathbf{F}_i = \int_S \{\boldsymbol{\sigma} \cdot \mathbf{n} - \rho \mathbf{u}[(\mathbf{u} - \mathbf{u}_i) \cdot \mathbf{n}]\} dS - \frac{d}{dt} \int_V \rho \mathbf{u} dV, \quad (22)$$

where  $S$  is a closed surface with outward unit normal vector  $\mathbf{n}$ , and  $V$  denotes the region which is inside the closed surface and outside the cylindrical body (see Fig. 3). As the cylindrical bodies were immobile, the velocities were  $\mathbf{u}_i \equiv \mathbf{0}$ . The integral in (22) was approximated by the quadrature of 400 points, and the radius of  $S$  was chosen as  $R + 2.6\Delta x$  for system A and as  $R + 2.0\Delta x$  for system B. The

**Table 1.**  
Systems of LB simulations

System	$\chi_1$	$\chi_2$	$R/\Delta x$	$L/\Delta x$	$h/\Delta x$	$(L_x/\Delta x) \times (L_y/\Delta x)$	$\kappa_F/(\Delta x)^2(\gamma_{LV}/10^{-4}\Delta x)$	$g/10^{-6}$	Number of time steps
A.1	0.5	0.5	7.9	32–72	0 <sup>a</sup>	400 × 50	0.8 (2.8)	5.0	810 000–1 290 000
A.2	−0.5	−0.5	7.9	32–72	−1.3 <sup>a</sup>	400 × 50	0.8 (2.8)	5.0	690 000–1 230 000
A.3	0.5	−0.5	7.9	32–72	−0.6 <sup>a</sup>	400 × 50	0.8 (2.8)	5.0	450 000–2 250 000
B	1	1	64.0	139–148	5 <sup>b</sup>	512 × 256	0.4 (3.9)	0	300 000

<sup>a</sup> The vertical position of the central axes of two cylinders, which was obtained from the LB simulations.

<sup>b</sup> The thickness of the liquid film around an isolated cylinder.

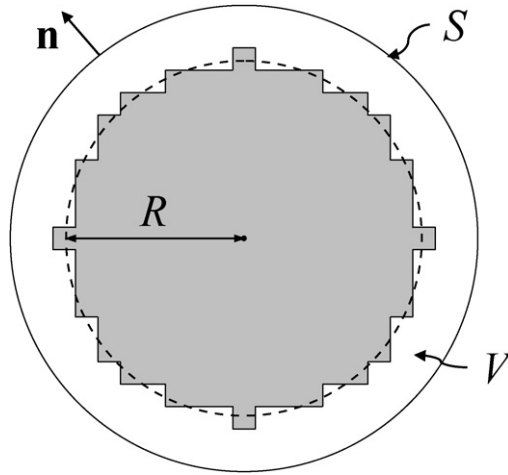


**Figure 3.** Cylindrical body of radius  $R$  (dashed line) approximately represented by a collection of lattice nodes (dark region).  $S$  represents a closed surface with outward unit normal vector  $\mathbf{n}$  and  $V$  denotes the fluid-phase region which is inside the closed surface and outside the cylindrical body. It is noted that this cylindrical body of  $R = 7.9\Delta x$  is identical to those for system A (see Figs 4–6).

values of  $\rho$ ,  $\mathbf{u}$  and  $\boldsymbol{\sigma}$  on  $S$  were calculated from the linearly interpolated values of  $f_i$  and  $g_i$  at the point on  $S$ .

The interaction force between the bodies 1 and 2, respectively centered at  $\mathbf{x}_1$  and  $\mathbf{x}_2$ , was given by:

$$F(L) = \frac{1}{2}(\mathbf{F}_1 - \mathbf{F}_2) \cdot \frac{\mathbf{x}_1 - \mathbf{x}_2}{|\mathbf{x}_1 - \mathbf{x}_2|}, \tag{23}$$

where  $L \equiv |\mathbf{x}_1 - \mathbf{x}_2|$  is the distance between the bodies. The interaction force is repulsive when  $F > 0$ , whereas it is attractive when  $F < 0$ .

Thus, the cylindrical bodies are approximated *via* rectangular steps. This approximation yields errors, the amount of which should decrease with increasing radius  $R$  of the cylinders. Indeed, as we will see below, a comparison between Fig. 7 (system A of  $R = 7.9\Delta x$ ) and Fig. 9 (system B of  $R = 64.0\Delta x$ ) will imply that the use of the larger  $R$  results in the better agreement between the LB and theoretical results. The amount of the errors is also affected by the applied relaxation times,  $\tau_f$  and  $\tau_g$ , in conjunction with the halfway bounce-back, no-slip boundary condition. This contribution is negligible in the present study, as far as the mechanically equilibrated systems are concerned.

2.4. Simulation details

Two types of capillary forces, lateral capillary force and capillary bridge force, were evaluated for systems A and B summarized in Table 1.



**2.4.1. Lateral capillary force (system A).** The simulation region was represented by the lattice nodes of  $L_x \times L_y = 400\Delta x \times 50\Delta x$  and confined within the solid walls. The wetting bottom wall of  $\chi = 1$  ( $\rho_S = \rho_L$ ) was placed at  $y = 0$  in the range of  $\Delta x \leq x \leq L_x$ , whereas the non-wetting upper wall of  $\chi = -1$  ( $\rho_S = \rho_V$ ) was located at  $y = L_y + \Delta x$  in the range of  $\Delta x \leq x \leq L_x$ . The sidewalls of  $\chi = 0$  ( $\rho_S = \rho_d$ ), which are in between wetting and non-wetting, were positioned at  $x = 0$  and  $L_x + \Delta x$ . The cylindrical bodies 1 and 2 of radius  $R = 7.9\Delta x$  were fixed at  $\mathbf{x}_1 = (L_x/2 - L/2, L_y/2)$  and  $\mathbf{x}_2 = (L_x/2 + L/2, L_y/2)$ , respectively. Three types of cylindrical body pairs were considered as summarized in Table 1: (A.1) two wetting bodies of  $\chi_1 = \chi_2 = 0.5$ , (A.2) two non-wetting bodies of  $\chi_1 = \chi_2 = -0.5$ , and (A.3) the wetting body of  $\chi_1 = 0.5$  and the non-wetting body of  $\chi_2 = -0.5$ . As an initial condition, the densities  $\rho_L$  and  $\rho_V$  were, respectively, given to the lower half ( $\Delta x \leq y \leq L_y/2$ ) and the upper half ( $L_y/2 + \Delta x \leq y \leq L_y$ ) of the simulation cell except the area of the solid bodies. The halfway bounce-back, no-slip boundary condition [9] was imposed on the fluid-side nodes of the walls and the body surfaces.

Every system was allowed to evolve until it reached mechanical equilibrium, when the separation  $L$  was given as in Table 1. The criterion for judging the mechanical equilibrium was:

$$\left| \frac{F(t_{n+1}) - F(t_n)}{F(t_{n+1})} \right| < 10^{-4}, \quad (24)$$

where  $F(t_n)$  is the force between the solid bodies calculated by (23) at time  $t_n = (30\,000n)\Delta t$  with positive integer  $n$ . The number of time steps required for equilibrating each system is listed in Table 1.

**2.4.2. Capillary bridge force (system B).** The simulation region was represented by the lattice nodes of  $L_x \times L_y = 512\Delta x \times 256\Delta x$ , and confined within the non-wetting rectangular box of size  $(L_x + 2\Delta x) \times (L_y + 2\Delta x)$  and wettability  $\chi = -1$ . The cylindrical bodies 1 and 2 of radius  $R = 64.0\Delta x$  and wettability  $\chi = 1$  were fixed at  $\mathbf{x}_1 = (L_x/2 - L/2, L_y/2)$  and  $\mathbf{x}_2 = (L_x/2 + L/2, L_y/2)$ , respectively. To cover the cylindrical bodies with the liquid films of thickness  $h = 5\Delta x$ , the density  $\rho_L$  was assigned to the lattice nodes located at  $R < |\mathbf{x} - \mathbf{x}_i| \leq R + h$  for  $i = 1$  and 2 as an initial condition, whereas the density  $\rho_V$  was given to the simulation cell except the area of the solid bodies and their liquid films. The halfway bounce-back, no-slip boundary condition [9] was imposed on the fluid-side nodes of the walls and the body surfaces. Once  $L$  was specified, the system was allowed to evolve over 300 000 time steps such that it reached mechanical equilibrium, where the left-hand side of (24) with  $t_n = n\Delta t$  was less than  $10^{-6}$ .

### 3. THEORETICAL DESCRIPTION

The following theoretical descriptions of the lateral capillary force (see Fig. 1) and the capillary bridge force between two cylindrical bodies (see Fig. 2) were applied to evaluate the results obtained from the LB simulations.

#### 3.1. Lateral capillary force

In the system depicted in Fig. 1,  $h_i$  is the vertical position of the central axis of cylinder  $i$  ( $=1$  or  $2$ ) with respect to the level  $y = \zeta(\pm\infty) \equiv 0$  of the non-disturbed horizontal interface far from the cylinders,  $\alpha_i$  is the three-phase contact angle, and  $\psi_i$  ( $\equiv \theta_i - \alpha_i$ ) and  $\psi'_i$  ( $\equiv \theta'_i - \alpha_i$ ) are the slope angles of the exterior and the interior menisci, respectively. The interaction force per unit length of cylinder 1 is a sum of contributions from the interfacial tension at the contact lines  $C_1$  and  $C'_1$  and from the asymmetrical hydrostatic pressure throughout the cylinder surface [33]:

$$F = -\gamma_{LV}[\cos(\theta'_1 - \alpha_1) - \cos(\theta_1 - \alpha_1)] - B\gamma_{LV}\left[\frac{1}{2}(\sin^2 \theta_1 - \sin^2 \theta'_1) + \frac{h_1}{R}(\cos \theta'_1 - \cos \theta_1)\right], \quad (25)$$

where:

$$B = q^2 R^2, \quad q^2 = \frac{(\rho_L - \rho_V)g}{\gamma_{LV}}. \quad (26)$$

Here,  $B$  and  $q^{-1}$  are called the bond number and the capillary length, respectively;  $B = 0.52$  and  $q^{-1} = 11.8\Delta x$  in the LB simulations of system A.

As the cylinders deform the fluid interface, the shape of the meniscus obeys the Laplace equation of capillary [1]:

$$\frac{d}{dx}\left[\frac{d\zeta/dx}{\sqrt{1 + (d\zeta/dx)^2}}\right] = \frac{(\rho_L - \rho_V)g\zeta}{\gamma_{LV}}, \quad (27)$$

where  $y = \zeta(x)$  is the equation of the deformed fluid interface. The upper surface of the liquid phase is flat far from the cylinders; this line is chosen as the level  $y = 0$  (see Fig. 1). Taking the interface shape  $\zeta$  and its slope  $\psi$  as variables, (27) yields in a parameterized form [1]:

$$-\frac{d(\cos \psi)}{d\zeta} = q^2 \zeta. \quad (28)$$

Theoretical descriptions for two interacting cylinders with the same wettability and those of opposite wettabilities are presented in Sections 3.1.1 and 3.1.2, respectively. Section 3.1.3 gives the numerical procedure to obtain the force-distance profiles.

**3.1.1. Cylinders with the same wettability.** Two cylinders of the same contact angle  $\alpha_1 = \alpha_2$  constrained at the same vertical position  $h_1 = h_2 = h$  are considered,

as shown in Fig. 1. In this case, the meniscus is symmetrical with respect to the line  $x = L/2$  [33].

After integration of (28) between  $-\infty$  ( $\zeta = 0, \psi = 0$ ) and  $C_1$  ( $\zeta = h_1 + R \cos \theta_1, \psi = \psi_1$ ), on the one hand, and between  $C'_1$  ( $\zeta = h_1 + R \cos \theta'_1, \psi = \psi'_1$ ) and M ( $\zeta = H, \psi = 0$ ), on the other, one gets the conditions for the interfacial equilibrium:

$$B \left( \frac{h_1}{R} + \cos \theta_1 \right)^2 = 2[1 - \cos(\theta_1 - \alpha_1)], \quad (29)$$

$$B \left[ \left( \frac{h_1}{R} + \cos \theta'_1 \right)^2 - \left( \frac{H}{R} \right)^2 \right] = 2[1 - \cos(\theta'_1 - \alpha_1)]. \quad (30)$$

The solution of (28) with the condition of  $\zeta = H$  at  $\psi = 0$  is:

$$q\zeta = [(qH)^2 + 2(1 - \cos \psi)]^{1/2}. \quad (31)$$

Equation (31) with the relation  $d\zeta/dx = -\tan \psi$  leads to:

$$\frac{d(qx)}{d\psi} = -\frac{\cos \psi}{[(qH)^2 + 2(1 - \cos \psi)]^{1/2}}. \quad (32)$$

Integrating (32) between  $C'_1$  and M yields the dimensionless horizontal distance between the three-phase lines  $C'_1$  and  $C'_2$  of the interior meniscus:

$$qd = \frac{2}{a} \left\{ (2 - a^2) \left[ F\left(a, \frac{\pi}{2}\right) - F\left(a, \frac{\pi - |\psi'_1|}{2}\right) \right] - 2 \left[ E\left(a, \frac{\pi}{2}\right) - E\left(a, \frac{\pi - |\psi'_1|}{2}\right) \right] \right\}, \quad (33)$$

where:

$$a^2 = \frac{4}{4 + (qH)^2}. \quad (34)$$

In the right-hand side of (33),  $F(a, \phi)$  and  $E(a, \phi)$  are, respectively, elliptic integrals of the first and second kind of modulus  $a$  and amplitude  $\phi$  [34]. The center-to-center distance between the two cylinders is given by:

$$qL = qd + 2B^{1/2} \sin \theta'_1. \quad (35)$$

*3.1.2. Cylinders with the opposite wettabilities.* For the sake of simplification, let us consider two cylinders of different contact angles,  $\alpha_1$  and  $\alpha_2 = \pi - \alpha_1$ , constrained at the same vertical position  $h_1 = h_2 = 0$ . In this case, the meniscus has an inflection point at M ( $x = L/2, \zeta = 0$ ), where the meniscus slope  $\psi = \beta$  [35]: the meniscus is symmetrical with respect to the inflection point, i.e.,  $\psi'_2 = -\psi'_1$  (or  $\theta'_2 = \pi - \theta'_1$ ).

After integration of (28) between  $-\infty$  ( $\zeta = 0, \psi = 0$ ) and  $C_1$  ( $\zeta = R \cos \theta_1, \psi = \psi_1$ ), on one hand, and between  $C'_1$  ( $\zeta = R \cos \theta'_1, \psi = \psi'_1$ ) and M ( $\zeta = 0$ ),

$\psi = \beta$ ), on the other, one obtains the equilibrium conditions:

$$B \cos^2 \theta_1 = 2[1 - \cos(\theta_1 - \alpha_1)], \quad (36)$$

$$B \cos^2 \theta'_1 = 2[\cos \beta - \cos(\theta'_1 - \alpha_1)]. \quad (37)$$

The solution of (28) with the condition of  $\zeta = 0$  at  $\psi = \beta$  is:

$$q\zeta = 2[\cos^2(\beta/2) - \cos^2(\psi/2)]^{1/2}. \quad (38)$$

Equation (38) with the relation  $d\zeta/dx = -\tan \psi$  leads to:

$$\frac{d(qx)}{d(\psi/2)} = -\frac{1 - 2\sin^2(\psi/2)}{[\cos^2(\beta/2) - \cos^2(\psi/2)]^{1/2}}. \quad (39)$$

Integrating (39) between  $C'_1$  and M yields:

$$qd = 2[F(b, \pi/2) - F(b, \phi'_1)] - 4[E(b, \pi/2) - E(b, \phi'_1)], \quad (40)$$

where:

$$b = \cos(\beta/2), \quad \sin \phi'_1 = \frac{\cos(\psi'_1/2)}{\cos(\beta/2)}. \quad (41)$$

The center-to-center distance  $L$  is given by (35) with (40).

**3.1.3. Numerical procedure.** We assume that the contact angle  $\alpha_i$  is equal to its static value given by  $\cos \alpha_i = \chi_i(3 - \chi_i^2)/2$  [31]. The vertical positions of the central axes of the cylinders are equal to  $h$  ( $=h_1 = h_2$ ) = 0,  $-1.3\Delta x$  and 0 for systems A.1, A.2 and A.3, respectively; the former two are the values obtained from the LB simulations as in Table 1, while the latter is the value assumed for the sake of simplification as in Section 3.1.2. If  $\alpha_1$  and  $h_1$  are thus specified,  $\theta_1$ , which determines the vertical location of the contact line of the outer meniscus on cylinder 1, is calculated from (29) or (36) with the additional condition that  $\zeta = h_1 + R \cos \theta_1$  has the same sign as  $\psi_1$  ( $\equiv \theta_1 - \alpha_1$ ).

Once  $\alpha_1$ ,  $h_1$  and  $\theta_1$  are given aforesaid, the force–distance profile is obtained numerically as follows. When  $\theta'_1$  is specified, the force  $F$  is directly calculated from (25). For systems A.1 and A.2,  $H$  is computed from (30),  $d$  from (33) with (34), and the center-to-center distance  $L$  from (35); for system A.3, on the other hand,  $\beta$  is calculated from (37) with the additional condition that  $\beta$  has the same sign as  $\psi'_1$  ( $\equiv \theta'_1 - \alpha_1$ ),  $d$  from (40) with (41) and  $L$  from (35).

### 3.2. Capillary bridge force

Figure 2 illustrates the capillary bridge of a liquid phase between two bodies, which leads to the interaction force between them. As in the case of the lateral capillary force [see (25) in Section 3.1], the capillary bridge force per unit length of each cylinder is a sum of contributions from interfacial tension at two lines M

and  $M'$ , and from the meniscus capillary pressure at the cross-section  $MM'$  [i.e.  $\gamma_{LV}(-1/r_1 + 1/\infty) = -\gamma_{LV}/r_1$  according to the Laplace equation]:

$$F = -2\gamma_{LV} + 2l \left( -\frac{\gamma_{LV}}{r_1} \right) = -2\gamma_{LV} \left( 1 + \frac{l}{r_1} \right). \quad (42)$$

It should be noted that the total capillary force  $F$  is independent of the choice of the cross-section [1].

If the volume of the capillary bridge remains constant,  $F$  of (42) is given as a function of the separation  $L$ . As this is not the case for the LB simulation of system B,  $F$  was estimated semitheoretically using both (42) and the simulation data as follows. The values of  $l$  and  $r_1$  for given  $L$  are determined by fitting the arc:

$$y - y_0 = l + r_1 - [r_1^2 - (x - x_0)^2]^{1/2}, \quad (43)$$

to the LB simulation result of the meniscus shape in the vicinity of  $M$ , where  $(x_0, y_0) \equiv (\mathbf{x}_1 + \mathbf{x}_2)/2$  is the midpoint of the central axes of two cylinders. Then, (42) with these values directly gives  $F$  for the specified  $L$ .

## 4. RESULTS AND DISCUSSION

In this section, the results of LB simulations defined in Table 1 under mechanical equilibrium are compared with the (semi)theoretical predictions given in Sections 3.1 and 3.2. Specifically, the separation distance dependence of the lateral capillary force and the capillary bridge force between two cylindrical bodies will be compared and analyzed in Sections 4.1 and 4.2, respectively.

### 4.1. Lateral capillary force

The snapshots of the fluid densities for systems A.1–A.3 including two cylindrical bodies are displayed in Figs 4–6, respectively, where the three panels correspond to the center-to-center distances of  $L = 32\Delta x$  (a),  $48\Delta x$  (b) and  $64\Delta x$  (c). Figures 4–6 illustrate that the liquid surface near the cylindrical bodies is deformed, depending on the wettabilities of the body surfaces: the wetting body of  $\chi_i = 0.5$  pulls up the liquid surface (i.e.  $\theta_i < \pi/2$ ), while the non-wetting body of  $\chi_i = -0.5$  pushes it down (i.e.  $\theta_i > \pi/2$ ). A comparison among three panels in Figs. 4–6 indicates that the liquid surface in the gap between the two cylinders is distorted more significantly with decreasing their separation, which results in the stronger interaction force exerted between the two cylinders, as will be mentioned below.

Figure 7 shows the lateral capillary forces between the two cylinders as a function of the separation  $L$  for systems A.1–A.3. The forces are attractive for systems A.1 and A.2, while those for system A.3 are repulsive. For every system, the force becomes stronger with decreasing  $L$ , which is explained by the degree of distortion of the liquid surface between the two cylinders (see Figs 4–6). The force–distance profiles of the LB simulation results reasonably agree with those of the theoretical

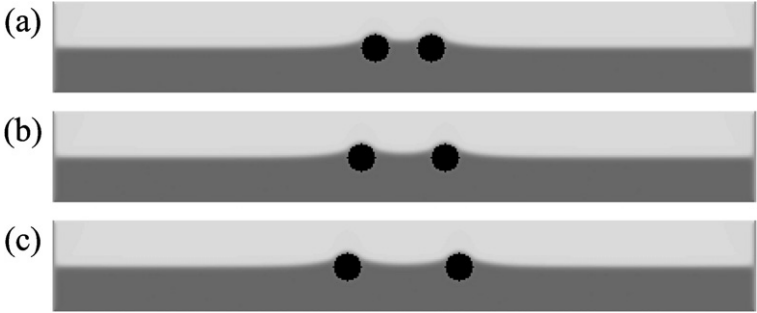


**Figure 4.** Snapshots of the fluid densities for system A.1 after mechanical equilibration: (a)  $L = 32\Delta x$  ( $qL = 2.7$ ), (b)  $L = 48\Delta x$  ( $qL = 4.1$ ) and (c)  $L = 64\Delta x$  ( $qL = 5.4$ ). Light gray indicates the vapor phase, dark gray represents the liquid phase and the black circles are the solid bodies. The top, bottom and side walls are depicted as the nodes with assigned fluid densities  $\rho_V$ ,  $\rho_L$  and  $\rho_d \equiv (\rho_L + \rho_V)/2$ , respectively.

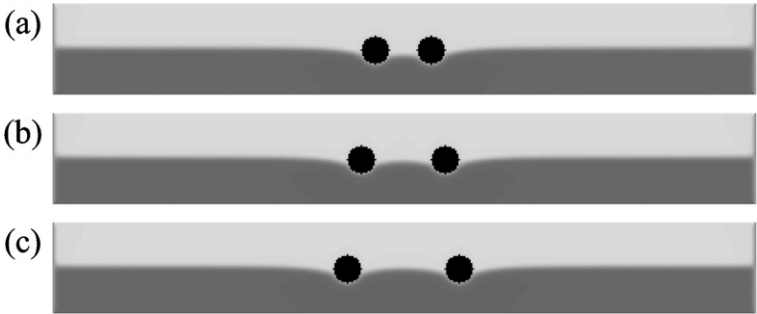


**Figure 5.** Same as Fig. 4, but for system A.2.

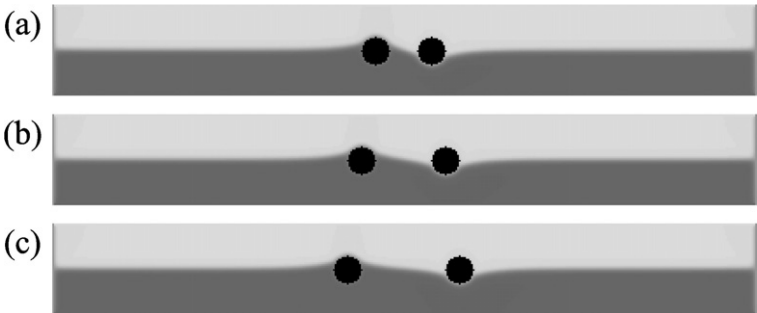


**Figure 6.** Same as Fig. 4, but for system A.3.

expression given in Section 3.1. Similar results are obtained in our previous LB study [20], where two square bodies on the liquid surface were simulated.

Figure 7 is recast in the semilogarithmic graph of Fig. 8. The forces exhibit an exponential decrease with the decay length of  $\lambda = 10.1\Delta x$ ,  $18.2\Delta x$  and  $11.9\Delta x$  for systems A.1–A.3, respectively, which were obtained by the fitting the relation

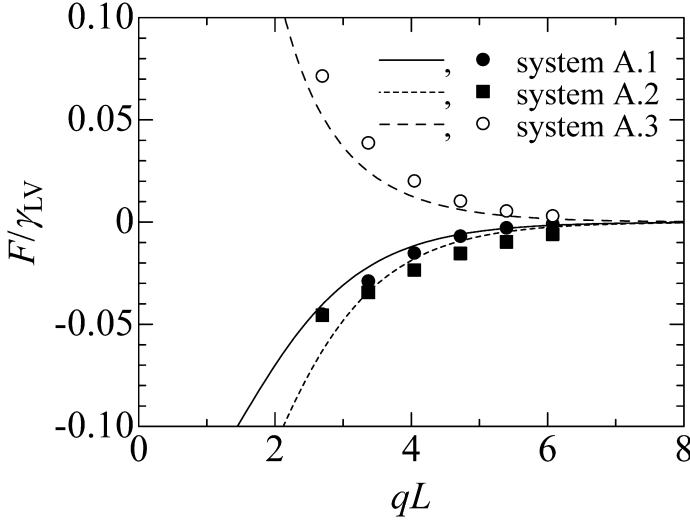


**Figure 7.** Forces between two horizontal cylinders as a function of the separation  $L$  for system A shown in Fig. 1 and Table 1: (●) system A.1,  $\chi_1 = \chi_2 = 0.5$ , (■) system A.2,  $\chi_1 = \chi_2 = -0.5$ , (○) system A.3,  $\chi_1 = -\chi_2 = 0.5$ . The distance is normalized by the capillary length  $q^{-1}$  obtained from (26). Three lines represent the theoretical force–distance profiles of (25) and (35) with the help of (29), (30), (33) and (34) for systems A.1 and A.2 or with the help of (36), (37), (40) and (41) for system A.3, where  $\gamma_{LV} = 2.8 \times 10^{-4} \Delta x$ ,  $g = 5.0 \times 10^{-6}$ ,  $\rho_L - \rho_V = 0.4$ ,  $R = 7.9 \Delta x$  and  $\cos \alpha_i = \chi_i(3 - \chi_i^2)/2$  are used; additionally,  $h = 0, -1.3 \Delta x$  and  $0$  are used for systems A.1–A.3, respectively (see also Section 3.1.3).

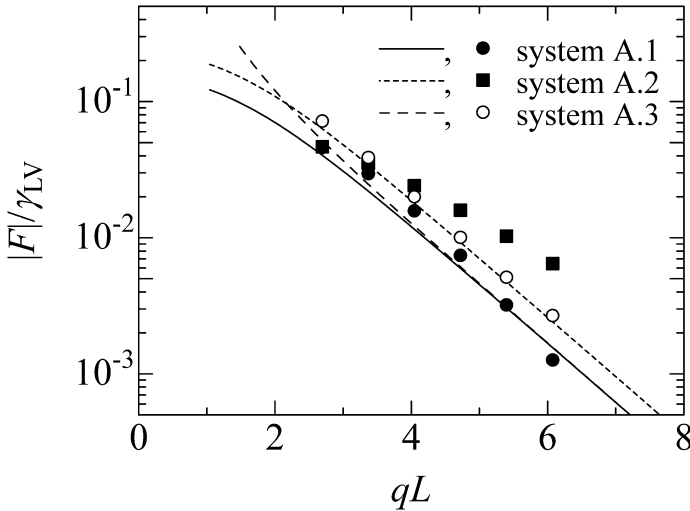


**Figure 8.** Same as Fig. 7, but recast in a semilogarithmic graph.

$|F| \sim \exp(-L/\lambda)$  to the simulation data of  $qL > 4$ ; in this region, the theoretical lines approximately exhibit the relation  $|F| \sim \exp(-qL)$ . The decay lengths are in good agreement with the capillary length  $q^{-1} = 11.8\Delta x$  obtained by (26), except for system A.2 (i.e. two non-wetting cylinders). In our previous study [20], similar discrepancy was observed for two non-wetting squares.

These results demonstrate that our LB simulations can capture the lateral capillary force between two cylindrical bodies, as well as that between two square bodies [20]. Nonetheless, the more detailed examination is necessary to understand why the decay length of the force between two non-wetting bodies is significantly larger than the capillary length. This will be addressed in a future publication.

#### 4.2. Capillary bridge force

Figure 9 shows the force between two cylinders covered with liquid films as a function of the separation  $L$  for system B. The interaction force remains almost zero at the distances  $L - 2R \geq 15\Delta x$ , where the two cylinders are sufficiently away from each other. When the two cylinders come closer, the force suddenly becomes attractive at  $L - 2R = 14\Delta x$ . This attractive force remains nearly constant in the region of  $11\Delta x \leq L - 2R \leq 14\Delta x$ .

To explain the origin of this attraction, the snapshots of the fluid densities for  $L - 2R = 11\Delta x, 14\Delta x, 15\Delta x$  and  $18\Delta x$  are displayed in Fig. 10(a–d, respectively). The corresponding profiles of the fluid densities in the plane including the central axes of two cylinders are shown in Fig. 11. A comparison between Fig. 10(b) and (c) and between the corresponding profiles in Fig. 11 indicates that

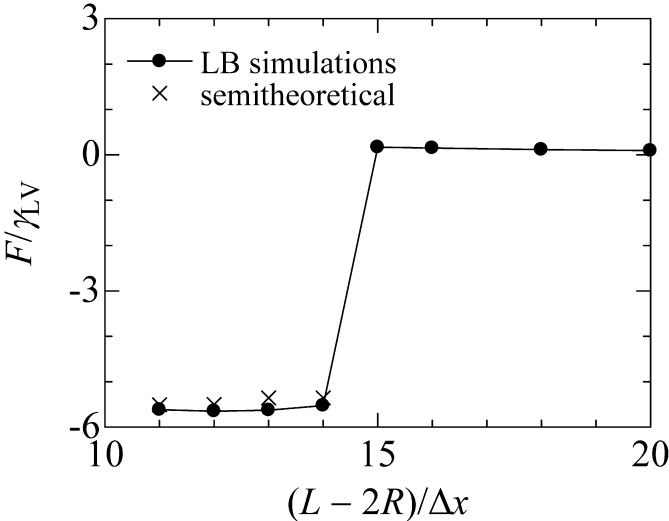


**Figure 9.** Force between two cylinders covered with liquid films as a function of the separation  $L$  for system B shown in Fig. 2 and Table 1: (●) LB simulations and (×) semitheoretical results of (42) with the help of (43) fitted to the simulation data (see also Section 3.2). The line is to guide the eyes.



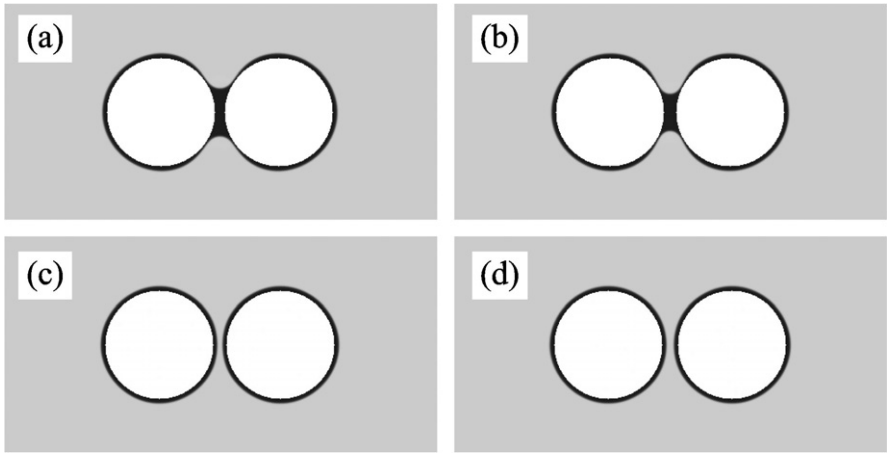


**Figure 10.** Snapshots of the fluid densities for system B after mechanical equilibration: (a)  $L - 2R = 11\Delta x$ ; (b)  $L - 2R = 14\Delta x$ , (c)  $L - 2R = 15\Delta x$  and (d)  $L - 2R = 18\Delta x$ . Light gray indicates the vapor phase, dark gray represents the liquid phase and the white circles are the solid bodies.

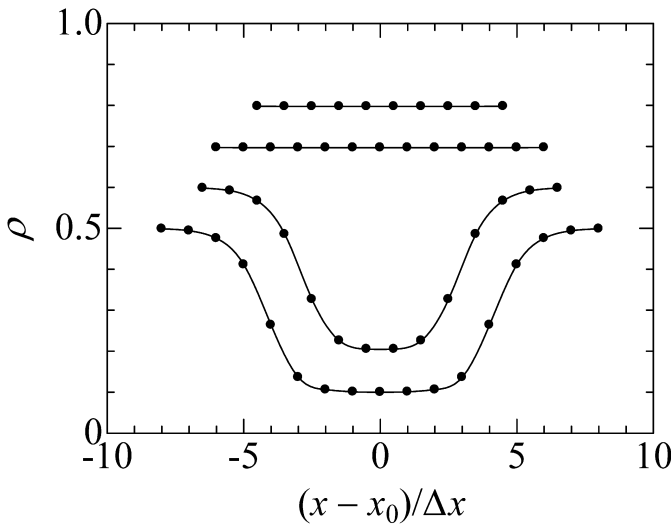


**Figure 11.** Profiles of the fluid densities in the plane ( $y = y_0$ ) including the central axes of two cylinders for system B of  $L - 2R = 11\Delta x$ ,  $14\Delta x$ ,  $15\Delta x$  and  $18\Delta x$ . The former three profiles are vertically shifted by 0.3, 0.2 and 0.1, respectively. Here,  $(x_0, y_0)$  indicates the midpoint of the central axes of two cylinders. The lines are to guide the eyes.

the attractive force in Fig. 9 is caused by the capillary bridge resulting from the fusion of two liquid films adsorbed on the cylinder surfaces. It is worth noting from the profile for  $L - 2R = 18\Delta x$  in Fig. 11 that (i) the thickness of the mechanically equilibrated liquid films on the cylinder surfaces is equal to  $h = 5\Delta x$ , where the liquid-vapor interface is defined as the region exhibiting the intermediate density

$\rho_d \equiv (\rho_L + \rho_V)/2 = 0.3$ , and that (ii) these liquid films are very thin and dominated by the interfacial region.

The capillary bridge forces in Fig. 9 coincide with the semitheoretical results of (42), demonstrating that our LB simulations can capture the capillary bridge force between two cylindrical bodies, as well as the lateral capillary force mentioned in Section 4.1.

## 5. CONCLUSIONS

Numerical simulations have been performed based on a two-dimensional two-phase LB method [28] to examine two types of capillary forces: (i) the lateral capillary force between two horizontal cylinders, constrained at a liquid–vapor interface, and (ii) the capillary bridge force between the two wetting cylinders covered with liquid films in vapor. It was found that the lateral capillary force between two cylindrical bodies is attractive when both bodies are wetting or non-wetting; in contrast, the force is repulsive when one is wetting and the other is non-wetting. The force–distance profile exhibits an exponential decrease for each body pair. For the capillary bridge force, it was successfully illustrated that the two cylinders must be located at sufficiently small separation distances to induce the formation of a liquid bridge and the consequent attractive force. These LB simulation results are in quantitative agreement with the results from the corresponding theoretical descriptions, except for the lateral capillary force between the non-wetting bodies.

The quantitative agreement between the simulation results and the theoretical predictions indicates that our LB method can reproduce the capillary interactions between two bodies of various wettabilities in a liquid–vapor two-phase fluid in mechanical equilibrium. Nonetheless, further examination is necessary to understand the discrepancy between the simulations and the theories of the capillary interaction for the non-wetting body pair. This will be addressed in the future, along with many-body effects and the impact of the hydrodynamic forces on bodies in the liquid–vapor flows.

## Acknowledgments

This work was partly supported by the Grants-in-Aid (no. 14750603/15206085) for Scientific Research from the Ministry of Education, Culture, Sports, Science and Technology in Japan, and by the Hosokawa Powder Technology Foundation, Japan.

## REFERENCES

1. P. A. Kralchevsky and K. Nagayama, *Particles at Fluid Interfaces and Membranes*. Elsevier, Amsterdam (2001).
2. P. A. Kralchevsky and K. Nagayama, Capillary interactions between particles bound to interfaces, liquid films and biomembranes, *Adv. Colloid Interface Sci.* **85**, 145–192 (2000).

3. P. A. Kralchevsky and N. D. Denkov, Capillary forces and structuring in layers of colloid particles, *Curr. Opin. Colloid Interface Sci.* **6**, 383–401 (2001).
4. N. B. Bowden, M. Weck, I. S. Choi and G. M. Whitesides, Molecule-mimetic chemistry and mesoscale self-assembly, *Acc. Chem. Res.* **34**, 231–238 (2001).
5. M. Yamaki, J. Higo and K. Nagayama, Size-dependent separation of colloidal particles in two-dimensional convective self-assembly, *Langmuir* **11**, 2975–2978 (1995).
6. K. D. Danov, B. Pouligny and P. A. Kralchevsky, Capillary forces between colloidal particles confined in a liquid film: the finite-meniscus problem, *Langmuir* **17**, 6599–6609 (2001).
7. D. H. Rothman and S. Zaleski, *Lattice-Gas Cellular Automata: Simple Models of Complex Hydrodynamics*. Cambridge University Press, Cambridge (1997).
8. B. Chopard and M. Droz, *Cellular Automata Modeling of Physical Systems*. Cambridge University Press, Cambridge (1998).
9. S. Succi, *The Lattice Boltzmann Equation for Fluid Dynamics and Beyond*. Clarendon Press, Oxford (2001).
10. S. Chen and G. D. Doolen, Lattice Boltzmann method for fluid flows, *Annu. Rev. Fluid Mech.* **30**, 329–364 (1998).
11. A. J. C. Ladd, Numerical simulations of particulate suspensions via a discretized Boltzmann equation. Part 1. Theoretical foundation, *J. Fluid Mech.* **271**, 285–309 (1994).
12. A. J. C. Ladd, Numerical simulations of particulate suspensions via a discretized Boltzmann equation. Part 2. Numerical results, *J. Fluid Mech.* **271**, 311–339 (1994).
13. C. K. Aidun, Y. Lu and E.-J. Ding, Direct analysis of particulate suspensions with inertia using the discrete Boltzmann equation, *J. Fluid Mech.* **373**, 287–311 (1998).
14. M. W. Heemels, M. H. J. Hagen and C. P. Lowe, Simulating solid colloidal particles using the lattice-Boltzmann method, *J. Comput. Phys.* **164**, 48–61 (2000).
15. N.-Q. Nguyen and A. J. C. Ladd, Lubrication corrections for lattice-Boltzmann simulations of particle suspensions, *Phys. Rev. E* **66**, 046708 (2002).
16. K. Stratford, R. Adhikari, I. Pagonabarraga and J.-C. Desplat, Lattice Boltzmann for binary fluids with suspended colloids, *J. Stat. Phys.* **121**, 163–178 (2005).
17. M. E. Cates, J.-C. Desplat, P. Stansell, A. J. Wagner, K. Stratford, R. Adhikari and I. Pagonabarraga, Physical and computational scaling issues in lattice Boltzmann simulations of binary fluid mixtures, *Philos. Trans. R. Soc. A* **363**, 1917–1935 (2005).
18. M. E. Cates, R. Adhikari and K. Stratford, Colloidal arrest by capillary forces, *J. Phys.: Condens. Matter* **17**, S2771–S2778 (2005).
19. K. Stratford, R. Adhikari, I. Pagonabarraga, J.-C. Desplat and M. E. Cates, Colloidal jamming at interfaces: a route to fluid-bicontinuous gels, *Science* **309**, 2198–2201 (2005).
20. H. Shinto, D. Komiyama and K. Higashitani, Lateral capillary forces between solid bodies on liquid surface: A lattice Boltzmann study, *Langmuir* **22**, 2058–2064 (2006).
21. A. K. Gunstensen, D. H. Rothman, S. Zaleski and G. Zanetti, Lattice Boltzmann model of immiscible fluids, *Phys. Rev. A* **43**, 4320–4327 (1991).
22. D. Grunau, S. Chen and K. Eggert, A lattice Boltzmann model for multiphase fluid flows, *Phys. Fluids A* **5**, 2557–2562 (1993).
23. X. Shan and H. Chen, Lattice Boltzmann model for simulating flows with multiple phases and components, *Phys. Rev. E* **47**, 1815–1819 (1993).
24. X. Shan and H. Chen, Simulation of nonideal gases and liquid–gas phase transitions by the lattice Boltzmann equation, *Phys. Rev. E* **49**, 2941–2948 (1994).
25. M. R. Swift, W. R. Osborn and J. M. Yeomans, Lattice Boltzmann simulation of nonideal fluids, *Phys. Rev. Lett.* **75**, 830–833 (1995).
26. M. R. Swift, E. Orlandini, W. R. Osborn and J. M. Yeomans, Lattice Boltzmann simulations of liquid–gas and binary fluid systems, *Phys. Rev. E* **54**, 5041–5052 (1996).

27. X. He, S. Chen and R. Zhang, A lattice Boltzmann scheme for incompressible multiphase flow and its application in simulation of Rayleigh–Taylor instability, *J. Comput. Phys.* **152**, 642–663 (1999).
28. T. Inamuro, Lattice Boltzmann method: a novel simulation method for fluid flows, *Bussei Kenkyu* **77**, 197–232 (2001) (in Japanese).
29. T. Inamuro, N. Konishi and F. Ogino, A Galilean invariant model of the lattice Boltzmann method for multiphase fluid flows using free-energy approach, *Comput. Phys. Commun.* **129**, 32–45 (2000).
30. A. J. M. Yang, P. D. Fleming III and J. H. Gibbs, Molecular theory of surface tension, *J. Chem. Phys.* **64**, 3732–3747 (1976).
31. D. Iwahara, H. Shinto, M. Miyahara and K. Higashitani, Liquid drops on homogeneous and chemically heterogeneous surfaces: a two-dimensional lattice Boltzmann study, *Langmuir* **19**, 9086–9093 (2003).
32. T. Inamuro, K. Maeba and F. Ogino, Flow between parallel walls containing the lines of neutrally buoyant circular cylinders, *Int. J. Multiphase Flow* **26**, 1981–2004 (2000).
33. C. Allain and M. Cloitre, Interaction between particles trapped at fluid interfaces. I. Exact and asymptotic solutions for the force between two horizontal cylinders, *J. Colloid Interface Sci.* **157**, 261–268 (1993).
34. M. Abramowitz and I. A. Stegun, *Handbook of Mathematical Functions, with Formulas, Graphs, and Mathematical Tables*. Dover, New York (1972).
35. H. M. Princen, The equilibrium shape of interfaces, drops, and bubbles. Rigid and deformable particles at interfaces, in: *Surface and Colloid Science*, E. Matijević (Ed.), vol. 2, pp. 1–84. Wiley-Interscience, New York (1969).